



MILD combustion versus conventional bluff-body flame of a premixed CH₄/air jet in hot coflow

G. Wang ^a, J. Si ^a, M. Xu ^b, J. Mi ^{a,*}

^a Department of Energy & Resources Engineering, College of Engineering, Peking University, Beijing, 100871, China

^b Marine Engineering College, Dalian Maritime University, Dalian, 116026, China



ARTICLE INFO

Article history:

Received 27 March 2019

Received in revised form

5 August 2019

Accepted 11 August 2019

Available online 12 August 2019

Keywords:

MILD combustion

Conventional combustion

Bluff body

Reaction zone

NO_x emission

ABSTRACT

The present work is to investigate the MILD (moderate and intense low-oxygen dilution) combustion of a premixed methane jet in hot coflow against its conventional counterpart, i.e., a typical bluff-body flame, under identical inlet and boundary conditions. This paper demonstrates that the MILD combustion develops as a stable 'flame' lifting far downstream from the nozzle while the conventional flame evolves immediately behind the bluff body. More specifically, all chemical reactions are found to occur far more slowly over a greatly larger reaction zone for the MILD combustion than for the conventional one. Also, for the MILD combustion, the laminar flame speed (S_L) is very small, far below the local flow speed (U_x), whereas chemical and mixing times are compatible so that the Damköhler number $Da \sim 1.0$. In contrast, the conventional combustion takes place with $S_L \geq U_x$ and $Da = 10-1000$. Moreover, the MILD combustion eventually emits little NO_x, only less than 3% of the emission from the conventional counterpart. Fundamentally, the MILD combustion produces the NO_x emission mainly through the N₂O-intermediate and NNH routes while the thermal NO_x mechanism dominates the conventional flame. In addition, this paper provides a comprehensive explanation to each of the above differences.

© 2019 Elsevier Ltd. All rights reserved.

1. Introduction

Combustion of fossil fuels currently provides around 80% of the traded energy generally in industrialized economies and will continue to be a major energy source for the foreseeable future. Simultaneously, the traditional combustion has been producing heavy emissions of carbon dioxide (CO₂), nitric oxides (NO_x) and fine particles (PM), and hence posing serious threats to our human life. An urgent action must be taken to reduce these emissions! Moderate or Intense Low-Oxygen Dilution (MILD) combustion has been found to be one of the most promising technologies for this action [1–3]. Comparing to traditional combustion (TC), the MILD combustion can be characterized by the uniform temperature field and invisible flame, and so it is often called flameless oxidation (FLOX) [2]. Likewise, in another fashion, its reactants (mostly the oxidant) usually have to be heated up to well above the auto-ignition temperature (T_{ai}) prior to entering the furnace, so it is also named high temperature air combustion (HiTAC) [3]. Two crucial characteristics of MILD combustion are the elevated

temperature of reactants and the reduced temperature rise in the combustion process [1].

Practically, internal or external exhaust gas recirculation (EGR) is commonly used to preheat incoming reactants and thus realize MILD combustion [4,5]. In the external EGR system, the recuperator and regenerator are usually used to absorb the waste heat of the flue gas and preheat the inlet reactants [3]. Comparing to traditional combustion processes, the thermal efficiency is higher in MILD combustion. Two reasons account for this. Firstly, the low peak temperature and the uniform furnace temperature reduce the irreversible heat loss in the combustion and heat transfer processes [6]. Secondly, the uniform temperature field and high flow speed in the furnace enhance the heat transfer, especially the radiative one [3]. Moreover, because the reactant temperature prior to the main reaction zone is higher than T_{ai} and the temperature rise is low, MILD combustion is more stable and produces much lower noise than traditional combustion [1].

Establishment of MILD combustion and its characteristics have been widely studied in recent years [7–14]. Weber et al. [7] examined the combustion characteristics of natural gas, heavy and light oils, and coal in highly preheated air in a semi-industrial scale furnace, finding that MILD combustion can be realized over a wide

* Corresponding author.

E-mail address: jmi@pku.edu.cn (J. Mi).

Nomenclature	
<i>Symbols</i>	
d	diameter of the premixed jet nozzle (mm)
Da	Damköhler number
$EINO$	NO emission index (g-NO/kg-fuel)
Fl	flame index
l_0	integral length scale (m)
l_k	Kolmogorov length scale (m)
m_{NOx}	NO _x mass flux (kg/s)
P	thermal power rate (kW)
Re	jet exit Reynolds number
Re_t	turbulent Reynolds number
S_L	laminar flame speed (m/s)
T_{ai}	auto-ignition temperature (K)
T_C	inlet temperature of the coflow (K)
T_J	inlet temperature of the premixed jet (K)
$\langle T \rangle$	Favre-averaged temperature (K)
$\langle T \rangle_{max}$	maximum Favre-averaged temperature in the whole computational domain (K)
T'	root-mean-squared temperature (K)
U_C	coflow velocity (m/s)
U_J	jet exit velocity (m/s)
U_x	axial velocity (m/s)
u'	root-mean-squared velocity (m/s)
V_R	reaction zone volume (m ³)
$V_{R,P}$	volume of the well-premixed reaction region (m ³)
X_i	mole-fraction of species i in the premixed jet or coflow
Y_i	mass fraction of species i after reaction
$\langle Y_i \rangle$	Favre-averaged mass fraction of species i after reaction
$\langle Y_i \rangle_{max}$	maximum Favre-averaged mass fraction of species i in the whole computational domain
Z	mixture fraction
$\langle Z \rangle$	Favre-averaged mixture fraction
<i>Greek letters</i>	
δ_L	laminar flame thickness (m)
ε	turbulent dissipation rate (m ² /s ³)
k	turbulent kinetic energy (m ² /s ²)
ν	kinematic viscosity (m ² /s)
τ_{flow}	characteristic flow time (s)
τ_{chem}	characteristic chemical time (s)
ϕ	local equivalence ratio
ϕ_J	equivalence ratio in the premixed jet
<i>Abbreviations</i>	
NBB	no-bluff-body
RZ	recirculation zone
WBB	with-bluff-body

range of fuels. Szegö et al. [8,9] experimentally investigated the effect of fuel dilution (diluting type and dilution level), heat extraction, air preheating and global equivalent ratio on the reaction zone characteristics and NO_x emissions on a parallel multi-jet MILD combustion burner system. They found that air preheating is not necessary to realize MILD combustion while heat extraction and fuel dilution is beneficial for the establishment of MILD combustion. NO_x emissions are less than 60 ppm and decrease with increasing heat extraction and fuel dilution level. Mi et al. [10] experimentally and numerically studied the performance of MILD combustion in a lab-scale furnace, varying the air-fuel momentum rate and air-fuel premixing. They concluded that there exists a critical momentum rate of the inlet reactants, below which MILD combustion cannot be realized. Mi et al. [11,12] also numerically investigated the effect of air and fuel nozzle diameter, air preheat temperature, fuel dilution, injection angle and injection separation of air and fuel on the establishment of non-premixed MILD combustion. They found that all parameters will influence the combustion characteristics through two crucial flow quantities, the recirculation ratio and the fuel-jet penetration distance. Li et al. [13] investigated the effect of fuel-air mixing pattern on the establishment of MILD combustion and reported that it is easy to realize MILD combustion in fully premixed condition but difficult in partially premixed condition. Recently, Kruse et al. [14] found that a high pressure increases NO_x emissions and hinders the establishment of MILD combustion in gas turbine.

Turbulent jet flame is a good experimental configuration for fundamental studies [15–21]. Dally et al. [15] studied the reaction characteristics of a turbulent CH₄/H₂ jet flame in hot coflow (JHC) and found that MILD combustion can be realized under low oxygen level. Cabra et al. [16,17] examined the lift-off behavior in a non-premixed H₂/N₂ and a premixed CH₄/air jet flame and revealed that the coflow temperature has a great impact on the flame lift-off height. Gkagkas et al. [18] investigated the combustion characteristics of the CH₄/air jet flame and found that the flame stabilization

is dominant by auto-ignition and the lift-off height has a significant sensitivity to the coflow composition. Wang et al. [19] numerically investigated the effect of coflow oxygen level ($X_{O_2, c}$) and temperature (T_C) on the realization of MILD combustion and finally proposed a useable classification of combustion regimes by $X_{O_2, c}$ and T_C . Mei et al. [20] (and Dai et al. [21]) studied the combustion characteristics of a methane jet flame in an O₂/CO₂ (and O₂/H₂O) coflow and reported that the oxy-fuel (and oxy-steam) reaction zone is larger than that in air-fuel combustion. Therefore, MILD combustion is expected to occur more easily for the JHC flame diluted by CO₂ or H₂O rather than by N₂.

Previous studies, e.g. Refs. [4–21], focused on the comparison of flameless MILD combustion and flame-visible combustion through varying inlet and boundary conditions, i.e., nozzle arrangement (e.g., ejection angle), inlet temperature and velocity, fuel type, fuel/oxidant diluting type and dilution level, furnace pressure and heat extraction degree. Those works were all on the establishment conditions and reaction characteristics of MILD and flame-visible combustion without using any flame stabilizers. On the other hand, designers of industrial burners and gas turbine combustors commonly use a bluff-body or multiple bluff-bodies to achieve stable traditional flames [22–25]. However, the MILD combustion has never been differentiated from a truly conventional flame. This stimulates the present work to characterize MILD combustion versus typical traditional combustion for applications. Additionally, previous works were mainly on non-premixed MILD combustion, while little work has been done on premixed MILD combustion [17,18], which is also very important in fundamental research and applications. So, a detailed comparison between premixed MILD combustion and traditional bluff-body combustion in methane jet flame is to be conducted in this work. More specifically, the present study uses identical inlet and outer boundary conditions for both cases of investigation but sets a conical bluff body near the jet nozzle exit to alter the inner flow structure for the traditional flame.

With the bluff body, the reactants are objected by the bluff body

and a stabilized flame is formed behind it [23–25]. Removing the bluff body, the premixed jet may be ignited far downstream by the hot coflow, and so MILD combustion may be established due to strong jet entrainment of vitiated coflow [15–17]. The aim of this work is to deeply investigate the differences between such MILD combustion and traditional bluff-body stabilized combustion. More specifically, the present study is to differentiate these two cases of combustion by distinguishing their flow fields, reaction zone characteristics and NO_x formations and thus emissions. The main objectives are:

- (1) To detail the establishment processes of the MILD combustion and traditional bluff-body stabilized combustion;
- (2) To understand the distinct reaction-zone characteristics and flame modes of the two combustion processes;
- (3) To quantify the NO_x formation and emissions routes from the two combustion processes.

2. Computational details

2.1. Numerical setup

The present calculations are based on the experimental configuration of the vitiated coflow burner (VCB) of Cabra et al. [17], as briefly described here. The VCB consists of a central jet nozzle

(inner diameter $d = 4.57$ mm) and a surrounding perforated plate with diameter of 210 mm. The central jet is a mixture of methane and air, with equivalent ratio $\Phi_j = 4.4$ and temperature $T_j = 320$ K. The surrounding plate was drilled with 2200 holes (1.58-mm diameter), on which premixed lean H₂/air flames were stabilized; their combustion products formed the vitiated coflow with bulk velocity $U_c = 5.4$ m/s and temperature $T_c = 1350$ K. The central jet nozzle extends 70 mm downstream of the perforated plate surface to ensure uniform coflow properties. The jet exit velocity (U_j) is 100 m/s, corresponding to the Reynolds number of $Re = 28000$. The other inlet conditions in the premixed jet and coflow are summarized in Table 1. Moreover, Cabra et al. [17] measured single-point temperatures and species mass fractions using the Raman-Rayleigh-LIF technique. Favre-averaged temperature and mass fractions of CH₄, H₂, O₂, H₂O, OH, CO and CO₂ and their fluctuations were computed. In addition, visible chemiluminescence was used to determine the flame front position and lift-off height.

For the present study, to compare MILD combustion and traditional bluff-body stabilized combustion, a hollow conical bluff body is placed at $x = 1.0d$ to form a conventional flame behind it, see Fig. 1. The jet exit velocity and coflow velocity are reduced to 50 m/s and 1 m/s, respectively, to stabilize the traditional flame in the recirculation zone. The coflow oxygen level of 6% (in volume) is taken to establish MILD combustion with no bluff-body. Three jet equivalent ratios ($\Phi_j = 0.8, 1.0$ and 1.2) are chosen to study the fuel-lean, stoichiometric and fuel-rich flames. The mole fraction of CH₄

Table 1
Inlet conditions of central premixed jet and hot coflow for all cases.

Cases	Central jet						Hot coflow				
	U_j (m/s)	T_j (K)	X_{CH_4}	X_{O_2}	X_{N_2}	Φ_j	U_c (m/s)	T_c (K)	X_{O_2}	X_{N_2}	X_{H_2O}
1 EXP	100	320	0.330	0.150	0.520	4.4	5.4	1350	0.12	0.15	0.73
2 NBB0.8 ^a	50	320	0.167	0.417	0.416	0.8	1.0	1250	0.06	0.94	0.00
3 NBB1.0	50	320	0.167	0.333	0.500	1.0	1.0	1250	0.06	0.94	0.00
4 NBB1.2	50	320	0.167	0.278	0.555	1.2	1.0	1250	0.06	0.94	0.00
5 WBB0.8	50	320	0.167	0.417	0.416	0.8	1.0	1250	0.06	0.94	0.00
6 WBB1.0	50	320	0.167	0.333	0.500	1.0	1.0	1250	0.06	0.94	0.00
7 WBB1.2	50	320	0.167	0.278	0.555	1.2	1.0	1250	0.06	0.94	0.00

^a NBB0.8 denotes no-bluff-body and $\Phi_j = 0.8$.

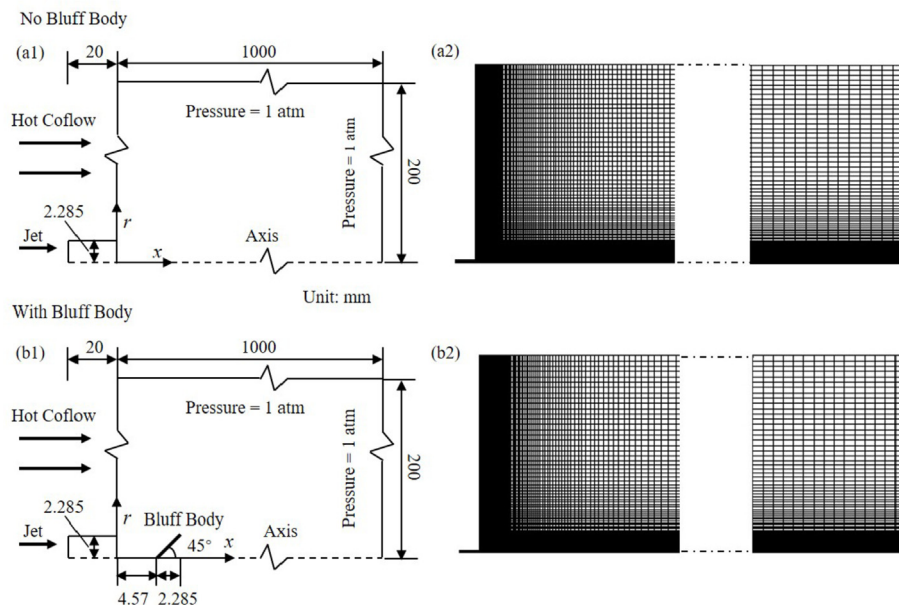


Fig. 1. Schematic diagram and orthogonal structured grid of the computational domain for the no-bluff-body (NBB) cases (a1, a2) and with-bluff-body (WBB) cases (b1, b2).

(X_{CH_4}) is kept constant for different Φ_j to keep the same power rate ($P = 4.9 \text{ kW}$). The detailed inlet conditions are also summarized in Table 1.

Considering the symmetry of the VBC configuration, a simplified two-dimensional (2-D) computational model is used to reduce computational cost. As shown in Fig. 1, the computational domain spans 1000 mm (about $219d$) axially and 200 mm (about $44d$) radially. The stretched structured grids with 14,600 cells and 20,000 cells are adopted for the cases of no-bluff-body (NBB) and with-bluff-body (WBB) after the verification of grid independency with a coarser grid of 6700 cells and a fine grid of 24,500 cells (see section 3.1). The smallest and largest grid sizes are $0.03d$ and $2.2d$, respectively.

2.2. Computational methods

The commercial software ANSYS Fluent 17.2 is currently used to solve the related transport equations, i.e., those of the mean mass conservation, axial and radial momentums, turbulent kinetic energy and its dissipation rate, Favre-averaged mass fractions for each species, radiation intensity and energy conservation. According to the previous studies [26,27], a modified $k-\epsilon$ model, i.e., adjusting $C_{1\epsilon}$ from 1.44 to 1.6, with the standard wall function, is adopted to emulate the turbulent flows. A Lagrangian particle-based Monte-Carlo method is used to solve the probability density function (PDF) transport equations of temperature and chemical compositions. The mixing model for the PDF equations is modified Curl (M-Curl) model, with modification of mixing constant to 2.3 according to the suggestion of Gkagkas et al. [18]. The particle number in each grid cell is 20. The detailed mechanism of GRI-Mech 2.11 [28], with 49 species and 279 reactions, is applied to simulate chemical reactions. Combining the transported PDF model and detailed mechanism is a good choice for modeling both MILD combustion [29] and traditional combustion [23]. To accelerate the computational process, we use the in situ adaptive tabulation (ISAT) model developed by Pope [30]. The ISAT tolerance is set to be 5×10^{-6} according to Masri et al. [31]. The discrete ordinate (DO) model [32] together with the weighted sum of gray gas model (WSGGM) is employed as the radiation model. The SIMPLE scheme is adopted for solving the pressure-velocity coupling. The second order upwind scheme is applied for spatial discretization to improve the accuracy of calculations. The convergence criteria are: (1) the residuals for energy and radiation equations are less than 10^{-6} and the residuals for

other equations are less than 10^{-5} and (2) the variations of the area-weighted outlet velocity and Favre-averaged temperature are less than 0.1 m/s and 1.0 K, respectively.

3. Model validation

3.1. Check to grid independency

To check the present mesh suitability, three orthogonal structured grids are used to model the experimental case (EXP). The cell number for the coarse, moderate and fine meshes are 6,700, 14,600 and 24,500, respectively. To quantify the mixed degree between the central premixed jet and the hot vitiated coflow, we adopt the mixture fraction (Z) defined by Bilger et al. [33] viz.

$$Z = \frac{2 \frac{Y_C - Y_{C,C}}{W_C} + \frac{1}{2} \frac{Y_H - Y_{H,C}}{W_H} - \frac{Y_O - Y_{O,C}}{W_O}}{2 \frac{Y_{C,I} - Y_{C,C}}{W_C} + \frac{1}{2} \frac{Y_{H,I} - Y_{H,C}}{W_H} - \frac{Y_{O,I} - Y_{O,C}}{W_O}} \quad (1)$$

where Y_i and W_i are the mass fraction and atomic mass of i th elements (C, H and O); $Y_{i,I}$ and $Y_{i,C}$ are the mass fractions of i th elements in the central jet and in the vitiated coflow, respectively.

Fig. 2 presents distributions of the axial velocity (U_x), Favre-averaged mixture fraction ($\langle Z \rangle$), Favre-averaged temperature ($\langle T \rangle$) and its root-mean-square (RMS) value (T'), and Favre-averaged species mass fractions (include main component $\langle Y_{O2} \rangle$ and minor component $\langle Y_{OH} \rangle$) on the centerline for the three grids. High consistency of the profiles of U_x and $\langle Z \rangle$ among these grids is evident. However, for the coarse mesh, the profiles of temperature and species concentrations are different with the other two grids. The positions of peak $\langle T \rangle$ and T' for the coarse mesh are about $10d$ downstream of those for the other two grids. And the sharp decline position of $\langle Y_{O2} \rangle$ is also delayed. Therefore, the reaction rates are underestimated and the ignition position is overestimated by the coarse mesh. Conversely, the results calculated with the moderate mesh are in line with those of the fine mesh. Therefore, the grid with 14,600 cells is adequate to model such a premixed jet flame in the vitiated coflow.

Fig. 3 displays the center-plane contours of Favre-average temperature ($\langle T \rangle$) and mass fraction of OH ($\langle Y_{OH} \rangle$) for the coarse, moderate and fine meshes. Evidently, the flame front occurs at $x \approx 35d$ for the moderate and fine meshes while it appears at $x \approx 42d$ for the coarse mesh. Moreover, the high temperature region ($>2100\text{K}$) and strong-reaction region ($\langle Y_{OH} \rangle$ over 0.002) of

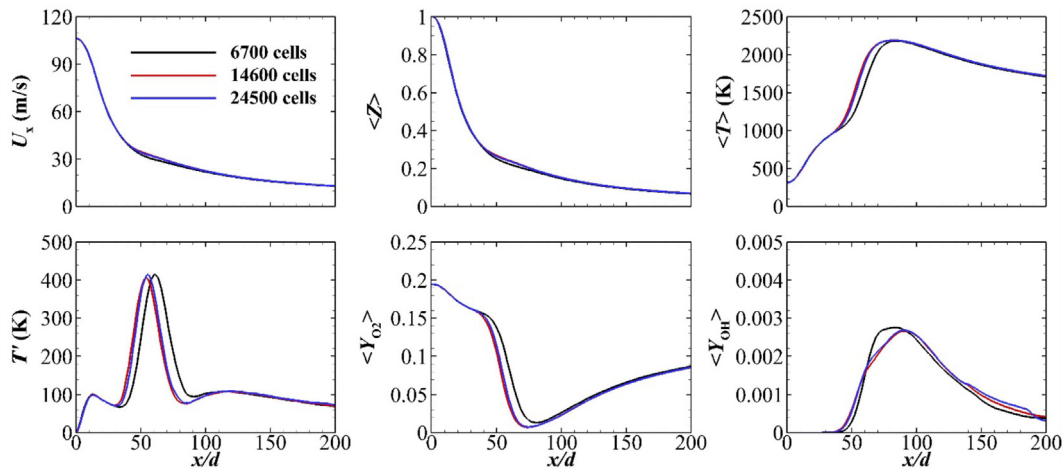


Fig. 2. Comparison of axial velocity (U_x) and Favre-averaged mixture fraction ($\langle Z \rangle$), Favre-averaged temperature ($\langle T \rangle$) and its root-mean-square value (T'), Favre-averaged mass fractions ($\langle Y_{O2} \rangle$ and $\langle Y_{OH} \rangle$) on the centerline for the three grids with 6,700, 14,600 and 24,500 cells, respectively.

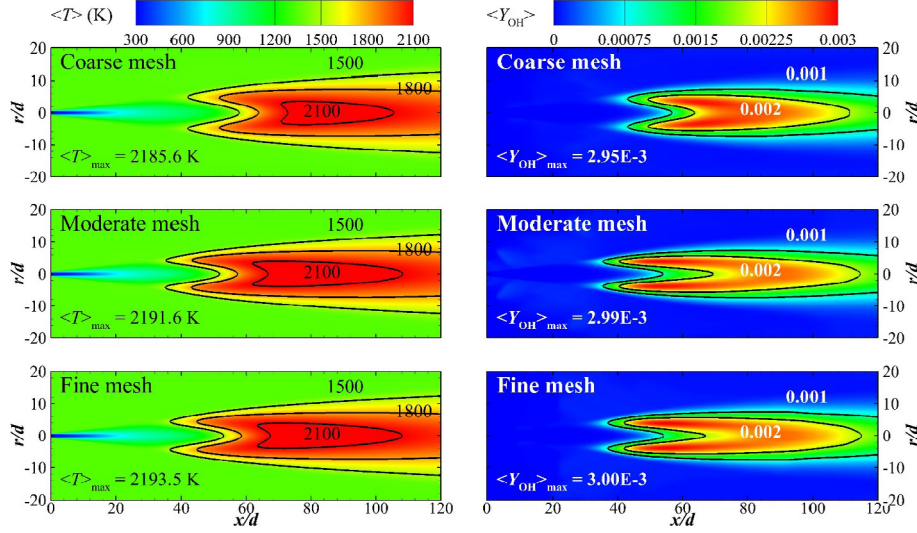


Fig. 3. Center-plane contours of Favre-average temperature ($\langle T \rangle$) and mass fraction of OH ($\langle Y_{OH} \rangle$) for the coarse, moderate and fine meshes.

the coarse mesh are smaller than those calculated with the moderate and fine meshes. The maximum Favre-averaged temperature $\langle T \rangle_{\max}$ and maximum Favre-averaged OH mass fraction $\langle Y_{OH} \rangle_{\max}$ are also underestimated by the coarse mesh. Therefore, the grid with 6700 cells is too coarse that it is not applicable for the calculation. Relatively, the results calculated with moderate grid are highly close to those of the fine mesh, with the differences in $\langle T \rangle_{\max}$ and $\langle Y_{OH} \rangle_{\max}$ less than 2K and 10^{-5} , respectively. So, the moderate grid with 14,600 cells is chosen for those calculations whose results are presented below.

3.2. Experimental validation

Present simulations, with the transported PDF model and fully detailed chemistry mechanism of GRI-Mech 2.11, are validated by the premixed CH₄/air jet flame experiment of Cabra et al. [17]. The measured and calculated Favre averaged mixture fraction ($\langle Z \rangle$), temperature ($\langle T \rangle$) and mass fractions of major and minor species ($\langle Y_{O_2} \rangle$, $\langle Y_{CO_2} \rangle$, $\langle Y_{CO} \rangle$ and $\langle Y_{H_2} \rangle$) are demonstrated in Fig. 4. Overall, the numerical results of $\langle Z \rangle$, $\langle T \rangle$, $\langle Y_{O_2} \rangle$ and $\langle Y_{CO_2} \rangle$ are in accordance with the experimental data. The predictions of $\langle Y_{CO} \rangle$ and $\langle Y_{H_2} \rangle$ agree well with the measurements at $x < 60d$. At $x > 60d$, the modeling slightly overvalues $\langle Y_{CO} \rangle$ and $\langle Y_{H_2} \rangle$. Cabra et al. [17] pointed out that this should be attributed to the little penetration of ambient air into the measurement region in the experiment.

Fig. 5 presents the radial distributions of the Favre-averaged mixture fraction ($\langle Z \rangle$), Favre-averaged temperature ($\langle T \rangle$) and its RMS value (T'). As clearly shown, the agreement between the modeled and measured profiles of $\langle Z \rangle$, $\langle T \rangle$ and T' is reasonably good, allowing some quantitative discrepancies for the temperature fluctuation T' in the downstream region. Therefore, the ignition

process of the premixed methane/air jet flame can be well captured by the present numerical model.

Above all, the current modeling settings have been validated to enable appropriate CFD simulations for the present study that predict the premixed flame characteristics.

4. Combustion establishment process

4.1. Global analysis on contour charts

Fig. 6 presents the center-plane contours of axial velocity (U_x) and Favre-averaged mixture fraction ($\langle Z \rangle$) and temperature ($\langle T \rangle$) for the no-bluff-body (NBB) and with-bluff-body (WBB) cases with jet equivalent ratio of $\Phi_j = 1.0$. For the NBB case, U_x and $\langle Z \rangle$ maintain high values (almost as high as those at the jet exit), see Fig. 6-a1 and 6-a2, for a considerably long distance (about 12d) as the premixed jet issues into the coflow. This region is so-called the jet “potential core” region. Combustion cannot be established here because of the extremely high local velocity (see Fig. 6-a3). Farther downstream, the central jet entrains a large amount of hot coflow, so that both U_x and $\langle Z \rangle$ decrease gradually with x . Within the entrainment process, the premixed reactants are simultaneously diluted and heated by the co-flowing low-oxygen mixture. The auto-ignition occurs once the reactant temperature has been elevated above the auto-ignition temperature ($T_{ai} = 813$ K), finally forming a stable lifted flame quite far away downstream from the nozzle exit (see Fig. 6-a4).

Alternatively, when a conical bluff body is placed downstream and near the jet exit, the premixed jet will be hindered and have to flow around the bluff body (see Fig. 6-b1). As a result, a recirculation zone (RZ) will form behind the bluff body, where a backflow

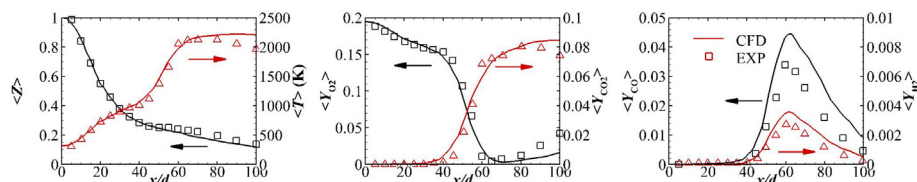


Fig. 4. Favre-averaged mixture fraction ($\langle Z \rangle$), temperature ($\langle T \rangle$) and mass fractions ($\langle Y_{O_2} \rangle$, $\langle Y_{CO_2} \rangle$, $\langle Y_{CO} \rangle$ and $\langle Y_{H_2} \rangle$) on the centerline. Solid lines represent numerical results (CFD). Hollow squares and triangles are experimental measurements (EXP).

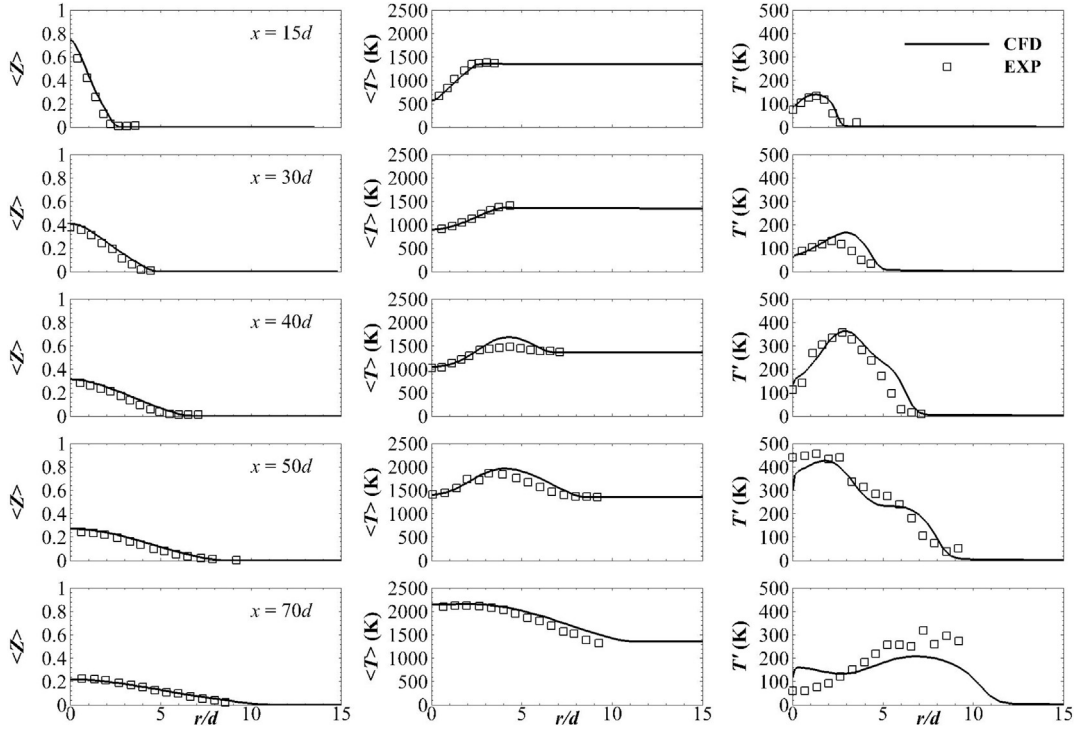


Fig. 5. Radial profiles of the Favre-averaged mixture fraction ($\langle Z \rangle$), Favre-averaged temperature ($\langle T \rangle$) and its root-mean-square value (T') at $x = 15d, 30d, 40d, 50d$ and $70d$. Solid lines represent numerical results (CFD). Hollow squares are experimental measurements (EXP).

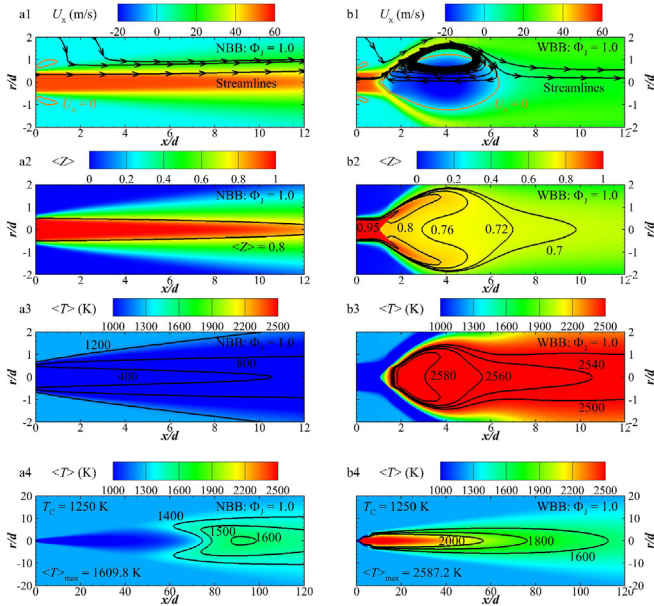


Fig. 6. Center-plane contours of axial velocity (U_x , a1 & b1), Favre-averaged mixture fraction ($\langle Z \rangle$, a2 & b2) and Favre-averaged temperature ($\langle T \rangle$, a3 & b3) in the near nozzle area and in the whole field (a4 & b4) for the no-bluff-body (NBB: $\Phi_j = 1.0$) and the with-bluff-body (WBB: $\Phi_j = 1.0$) cases.

occurs. Correspondingly, most of the premixed reactants will be trapped and thus stay in the RZ for a sufficiently long period of time, which may be treated approximately as the residence time [22]. In such conditions, high temperature patching (replicating the spark ignition in experiments) is used to ignite the reactants in the RZ and thus to develop a flame there. This flame then continuously ignites

the incoming reactants and acts as a stable flame of the expanded recirculation zone (see Fig. 6-b3 and 6-b4).

For the NBB case, the central jet is slowly heated by the hot coflow (1250 K) when flowing downstream and finally the 'flame' is stabilized at about $x = 50d$. At that position, the premixed reactants have been fully diluted by the low-oxygen coflow (6% in volume). The maximum temperature is about 1600 K, corresponding to a temperature rise of about 350 K, thus it falls in the mode of MILD combustion. In contrast, for the WBB case, the mixing process is greatly intensified by the bluff body (see Fig. 6-b2). The premixed jet is simultaneously diluted by the high temperature combustion products in the RZ and by the hot coflow outside, so the mixture fraction decreases quickly and temperature rises promptly. Thus, the reactants are immediately burnt in the RZ and then flame stabilizes and heat rapidly releases there. The maximum temperature is over 2580K and the combustion is a typical conventional flame.

To conclude, the ignition processes are totally different for the NBB and WBB cases. For the NBB case, the premixed reactants are heated and diluted by the hot vitiated coflow, then auto-ignition occurs and stable lifted MILD combustion "flame" is formed. However, for the WBB case, the incoming premixed reactants are continuously ignited by the high temperature combustion products in the RZ, so a conventional flame is stabilized behind the bluff body. Next, we will further discuss the ignition processes of these two regimes using the scatterplots at different axial locations.

4.2. Scatterplot analysis

To compare the two combustion processes insightfully, the scattered data of temperature (T) and mass fraction of OH (Y_{OH}) against the mixture fraction (Z) and the local equivalence ratio (Φ) are plotted in Figs. 7 and 8. (To inspect very small Y_{OH} properly, logarithm is used for Y_{OH} in Fig. 8. Both Z and Φ are 1.0 in the premixed jet and 0.0 in the vitiated coflow. So, they both range from

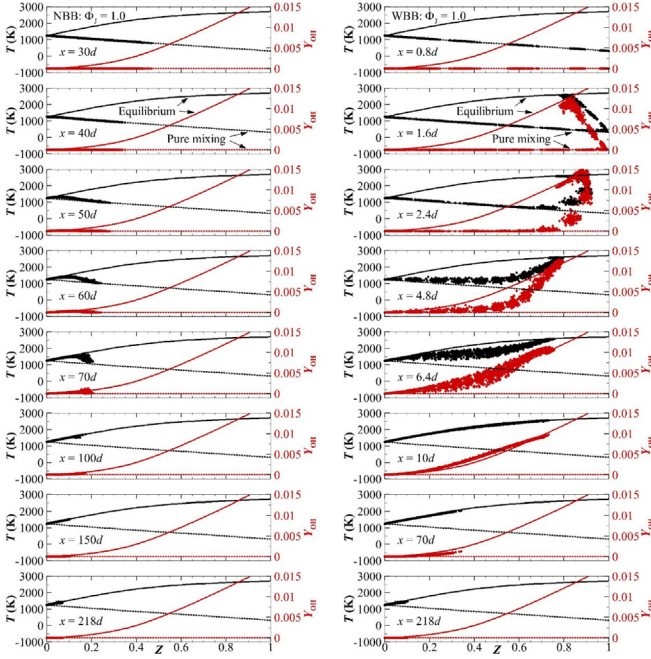


Fig. 7. Scatterplots of temperature (T , black dots) and OH mass fraction (Y_{OH} , red dots) against the mixture fraction (Z) at different x for the no-bluff-body (NBB: $\Phi_J = 1.0$) and with-bluff-body (WBB: $\Phi_J = 1.0$) cases. The pure mixing and chemistry equilibrium lines are calculated in a perfectly stirred reactor (PSR).

0.0 to 1.0.) Such scatterplots represent the joint distributions of T and Y_{OH} with Z and ϕ that help us to understand the scalar structure of the flame. Of note, we select data from 100 iteration steps, with the step interval of 10 iterations, to draw the scatterplots; and each data ensemble is produced by combining the whole radial profile at each axial location. For reference, the curves of the pure mixing and equilibrium temperature and Y_{OH} from perfectly stirred reactor (PSR) calculations are also plotted. Pure mixing means mere mixing of the premixed jet with hot coflow without any reaction while equilibrium represents fully chemical reactions.

For the NBB case, all temperature points fall on the purely mixing line with $Y_{OH} = 0$ at $x \leq 30d$, which means that no reactions occur in the region upstream of $x = 30d$. At $x = 40d$, tiny OH appears at $\phi \leq 0.4$ (see Fig. 8), indicating the occurrence of auto-ignition from here. From $x = 50d$ to $70d$, the temperature and OH points fall on the equilibrium line at low Z or ϕ values, and this portion widens as x increases. However, near the high end of Z or ϕ , the points fall between the pure mixing and equilibrium line. Farther downstream at $x = 100d$, almost all temperature and OH samples reach the equilibrium line, reflecting the fully chemical reactions and heat release there. The combustion event occurs in a long region from about $40d$ to $<150d$. During this process, auto-ignition firstly occurs at lower Z or ϕ (mixing layer) for higher initial temperatures and shorter ignition delay there, then the 'flame front' propagates toward higher Z or ϕ (central jet, Fig. 6-a4), agreeing well with the results of Cabra et al. [16,17]. Farther downstream at $x = 150d$ (see Fig. 8), chemical reactions become weak with reactants burning out, so all the OH points drop off the equilibrium line. It is interesting to see that all the temperature points still lie along the equilibrium line perhaps because of a very low rate of heat transfer from the reaction region to the hot coflow. At the end of the computational domain ($x = 218d$), low OH concentration exists at $Y_{OH} < 10^{-4}$ (see Fig. 8), indicating some very weak combustion is still going on.

For the WBB case, distributions of scatter points are totally

different in the near field because the bluff body considerably enhances the turbulent mixing and accelerates chemical reactions through a recirculating zone (RZ) behind it. At $x = 0.8d$, all temperature and OH points at $0 \leq Z, \phi \leq 1$ fall on the pure mixing line, indicating no reaction and heat release here. At $x = 1.6d$, i.e., the end of the bluff body, the premixed reactants mix with both the extremely hot combustion products in the recirculation zone with $Z \approx 0.8$ and the vitiated coflow outside with $Z = 0$ (see Fig. 6-b2). That is, there are two mixing layers. It follows that the temperature and OH samples split into two branches. The lower-temperature branch occurs over a wide range of Z (from 0.0 to about 1.0) and follows the line of pure mixing, representing the nonreactive mixing between the premixed jet and the vitiated coflow. The maximum Z is about 1.0 because there are still some premixed reactants that are almost totally undiluted (see Fig. 6-b2). The other branch occurs at $0.8 \leq Z \leq 1$ and belongs to the mixing process between the premixed jet and the central RZ combustion products of extremely high temperature (>2500 K, see Fig. 6-b2). Chemical reactions in the RZ take place so rapidly that the temperature and Y_{OH} scatter points for the combustion products distribute on both lean and rich-fuel equilibrium lines, ranging the temperature (and Y_{OH}) between 320 K and about 2600 K (0 and about 0.013). Downstream to $x = 2.4d$, the premixed reactants are diluted and thus the maximum Z decreases to about 0.92. Within the dilution process, more premixed reactants are heated and also ignited rapidly by the RZ combustion products ($T > 2500$ K). Consequently, new reactions begin at $Z \geq 0.7$ so that many samples for temperature and OH move away from the purely mixing line. Worth noting is that some scatter points are still kept on the equilibrium lines at $0.76 \leq Z \leq 0.88$. The recirculation carries low- Z gases upstream and thus extends Z to 0.76. The RZ flame propagates across the mixing layer between the combustion products and the premixed reactants, thus extending Z to 0.88. Farther downstream at $x = 4.8d$, the premixed jet is well diluted and the two mixing layers join up. All temperature and OH points except their peak values are between the mixing line and the equilibrium line. As x increases to 6.4d, they move closer to the lean-fuel equilibrium line. At $x = 10d$, all the reactive gases across the jet are fully mixed, so that all temperature and OH points fall on the chemical equilibrium line. Farther downstream, all the reactants are burning out. At $x = 70d$ (see Fig. 8), chemical reactions weaken dramatically and OH points drop off the equilibrium line. Similar to the NBB case, all the temperature points still lie along the equilibrium line because heat transfers at a very low rate from the central region to the hot coflow. At $x = 218d$ (computational domain end, Fig. 8), Y_{OH} becomes nearly zero, indicating the end of chemical reactions.

5. Reaction zone characteristics

5.1. Reaction zone

Following the work of Mei et al. [20,27], we consider the contour of $R_{CO} = 0.05$ as the boundary of the reaction zone, where R_{CO} is defined by

$$R_{CO} = \langle Y_{CO} \rangle / \langle Y_{CO} \rangle_{max} \quad (2)$$

where $\langle Y_{CO} \rangle_{max}$ is the maximum Favre-averaged CO mass fraction in the whole computational domain. Fig. 9 demonstrates the contour distributions of Favre-averaged CO mass fraction ($\langle Y_{CO} \rangle$) for the no-bluff-body (NBB: $\Phi_J = 0.8, 1.0$ and 1.2) and with-bluff-body (NBB: $\Phi_J = 0.8, 1.0$ and 1.2) cases. Several observations can be made from the plots. Firstly, for the NBB case, the CO levels are less than those of WBB case by one to two orders of magnitude, indicating that reactions occur much more rapidly in the WBB case.

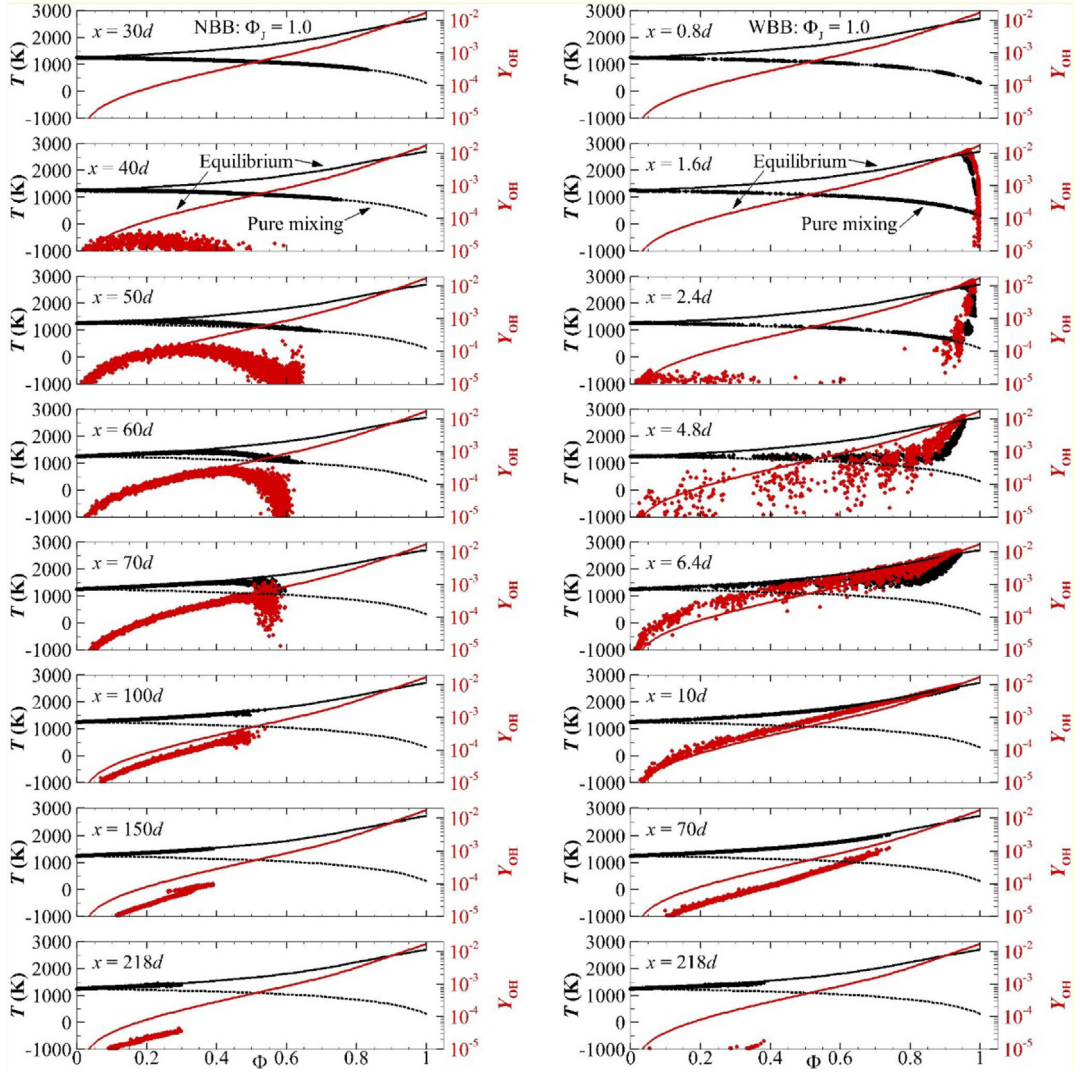


Fig. 8. Scatterplots of temperature (T , black dots) and OH mass fraction (Y_{OH} , red dots) against the local equivalence ratio (ϕ) at different indicated x values for the no-bluff-body (NBB: $\Phi_j = 1.0$) and with-bluff-body (WBB: $\Phi_j = 1.0$) cases. The pure mixing and chemistry equilibrium lines are calculated in a perfectly stirred reactor (PSR). Note that Y_{OH} is shown in logarithmic scale to facilitate the observation to very small values of Y_{OH} .

Secondly, $\langle Y_{CO} \rangle_{max}$ decreases with increasing Φ_j for the NBB case, but the trend is totally reversed for the WBB case. This is due to different reaction patterns for the WBB and NBB cases. For the WBB case, the $\langle Y_{CO} \rangle$ peak appears in the recirculation zone and only the incoming premixed reactants can affect the reactions there (the vitiated coflow has no impact). As Φ_j increases, the oxygen in the jet becomes deficient or the jet becomes lean-fuel, so CO will accumulate behind the bluff body and $\langle Y_{CO} \rangle_{max}$ arises. However, for the NBB case, the premixed reactants are mixed and diluted by the low-oxygen coflow as x increases, so the deficient oxygen is replenished. Moreover, as Φ_j increases, the complete combustion of the premixed reactants requires the NBB jet to entrain more oxygen from the coflow over a longer distance, hence resulting in more dilution. Therefore, in the NBB case, the increase of Φ_j slows combustion reactions and so decreases $\langle Y_{CO} \rangle_{max}$.

Thirdly, the reaction zone (bounded by the black line) is much larger for the NBB case comparing to the WBB case. The lower temperature and slower reactions caused by the strong dilution of the low-oxygen coflow mean that the reactants need more time and space to burn out. Therefore, the reaction zone is significantly enlarged for the NBB case.

5.2. Burning mode

To further analyze the burning mode in the reaction zone, we use the flame index (FI) defined by Yamashita et al. [34] as

$$FI = \frac{\nabla \langle Y_F \rangle \cdot \nabla \langle Y_O \rangle}{|\nabla \langle Y_F \rangle| |\nabla \langle Y_O \rangle|} \quad (3)$$

where $\nabla \langle Y_F \rangle$ and $\nabla \langle Y_O \rangle$ are the gradients of the Favre-averaged mass fractions of fuel ($\langle Y_{CH4} \rangle$) and oxygen ($\langle Y_{O2} \rangle$), respectively. The value of FI is between -1 and 1 , where $FI = 1$ represents a fully premixed flame and $FI = -1$ stands for a fully non-premixed flame. Therefore, we assume that when $FI \geq 0.5$, the flame is a well premixed flame; when FI is between -0.5 and 0.5 , it is a partially premixed flame; when $FI \leq -0.5$, it is a non-premixed flame. Note that originally FI is not related to combustion reactions. Only if there is a flame, FI can be used to decide what kind of flame it is. Hence, we will use it only in the reaction zone. It is also important to note this: for the NBB and WBB cases, although the reactants are initially fully mixed and thus issue as a premixed jet, the MILD combustion and traditional bluff-body flame cannot be treated as a

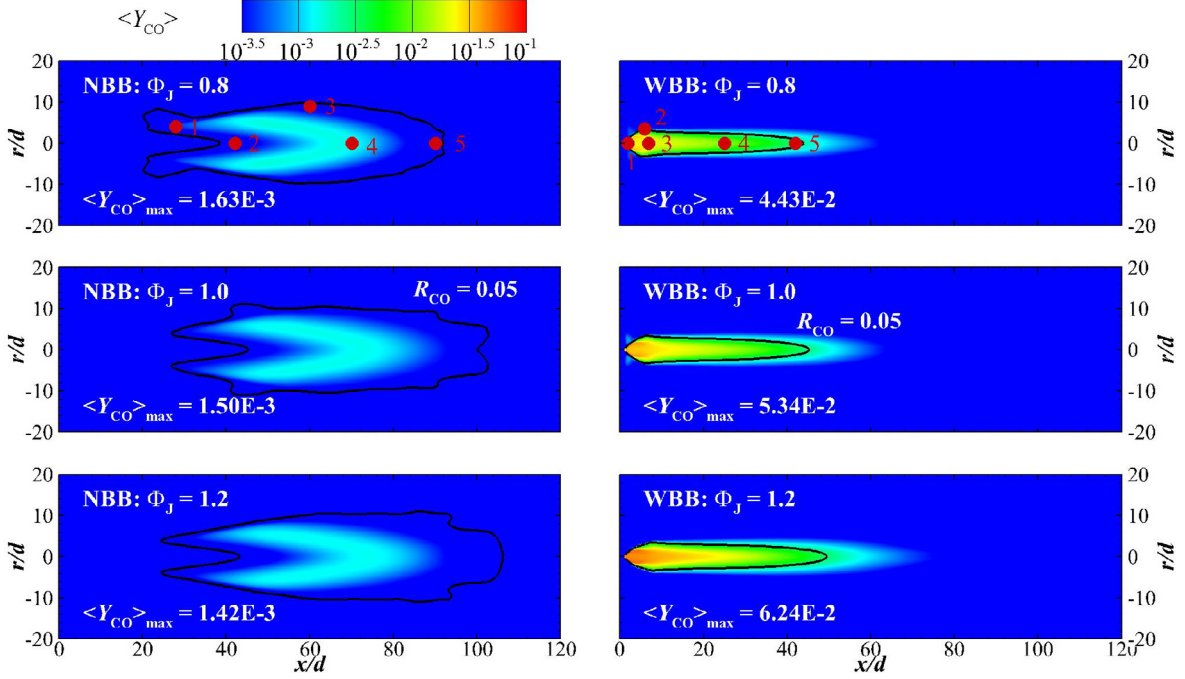


Fig. 9. Center-plane contours of Favre-averaged CO mass fraction ($\langle Y_{CO} \rangle$) for the no-bluff-body (NBB: $\Phi_J = 0.8, 1.0$ and 1.2) and with-bluff-body (WBB: $\Phi_J = 0.8, 1.0$ and 1.2) cases. Black lines correspond the boundaries of the reaction zones. Red dots are typical points selected for later flame classification. The maximum Favre-averaged CO mass fractions ($\langle Y_{CO} \rangle_{max}$) are also shown on the plots.

fully premixed flame. This is because the accomplished combustion processes have to be involved by the turbulent mixing between the premixed jet and hot coflow.

Fig. 10 demonstrates the contour distributions of flame index (FI) in the reaction zone for the NBB and WBB cases. The dashed black lines are the boundaries of the reaction zone at which $R_{CO} = 0.05$, while the white solid lines represent contours of $FI = 0.5$. As expected, no non-premixed flame occurs in both WBB and NBB cases where FI is above -0.5 in the whole reaction zone. Clearly, the distributions of FI show totally different characteristics for the NBB and WBB cases. For the NBB case, the premixed jet is slowly diluted by the hot coflow and so can maintain high speed

and high Z when flowing downstream. The NBB turbulent mixing is not strong when comparing to the WBB case. Moreover, $\nabla(Y_F)$ and $\nabla(Y_O)$ are almost in the same direction so that $\nabla(Y_F) \cdot \nabla(Y_O)$ is high and $FI > 0.5$ for $x \leq 70d$ in the NBB case at $\Phi_J = 0.8$. Farther downstream, FI decreases to less than 0.5 due to the entrainment of large amount of low-oxygen coflow and the different gradient directions of fuel and oxidant. So, the flame becomes partially premixed flame. Within the whole reaction zone, the well premixed flame accounts for a large proportion. In addition, as Φ_J increases, the well premixed 'flame' region shifts downstream together with the whole reaction zone.

For the WBB case, the turbulent mixing is intensified by the bluff

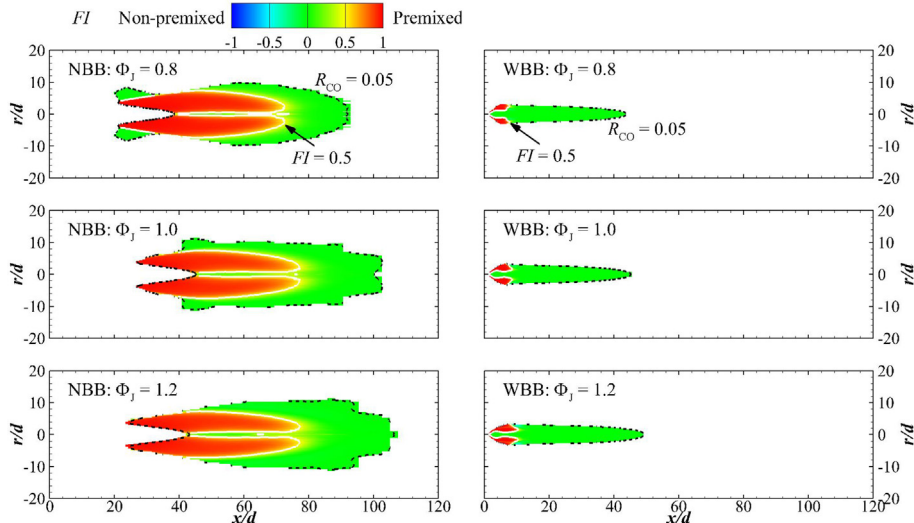


Fig. 10. Center-plane contours of the flame index (FI) in the reaction zone for the NBB and WBB cases at $\Phi_J = 0.8, 1.0$ and 1.2 . Solid white lines represent the contours of $FI = 0.5$. Dashed black lines correspond to the reaction zone borders at $R_{CO} = 0.05$.

body, so the mixing process of the premixed jet with combustion products in the recirculation zone (RZ) and with the vitiated coflow are both greatly enhanced. So, the gradient directions of fuel and oxidant are disordered and FJ is low. Therefore, the partially premixed flame region is quite large and the well premixed flame region is confined near to the edge of the RZ. Similar to the NBB case, the increase of ϕ_j makes both WBB flame regions to move downstream.

To quantify the combustion characteristics in the reaction zone, the reaction zone volume (V_R) and the ratio of the premixed reaction zone ($V_{R,P}/V_R$) are calculated and exhibited in Fig. 11(a) and (b), respectively. Evidently, the reaction zone volume for the NBB case is about 0.0015 m^3 for $\phi_j = 0.8$, which is 22 times as that for the WBB case. As ϕ_j increases, the oxygen fraction in the premixed jet reduces, so the fuel needs to entrain more oxidant from the low-oxygen coflow to burn out and thus V_R increases for both NBB and WBB cases. More specifically, the ratio of NBB volume to WBB volume reduces slightly with increasing ϕ_j .

Fig. 11b shows that the proportion of the mainly premixed part, $V_{R,P}/V_R$, is about 0.4 for the NBB case at $\phi_j = 0.8$, which is more than twice of that for the WBB case (about 0.15). This difference can be explained. In the WBB case, the turbulent mixing is strengthened by the bluff body and the directions of $\nabla\langle Y_F \rangle$ and $\nabla\langle Y_O \rangle$ are disordered. Therefore, $\nabla\langle Y_F \rangle \cdot \nabla\langle Y_O \rangle$ is low and the mainly premixed part is quite small relative to the whole reaction zone (see Fig. 10). As ϕ_j increases, the ratio $V_{R,P}/V_R$ decreases significantly for the NBB case and increases slightly for the WBB case. This can be attributed to different conditions of flow, mixing and reactions for the two cases. For the NBB case, the reaction zone becomes larger with increasing ϕ_j , but the mainly premixed part remains nearly unchanged for the

similar entraining and mixing conditions, so the premixed proportion decreases. However, the situation changes for the WBB case: as ϕ_j increases, the overall oxidation weakens and the temperature reduces (see Fig. 14a). Thus, both turbulent mixing processes of the premixed reactants with the RZ combustion products and with hot coflow become weakened. So, for the WBB case, the increase of ϕ_j enlarges the premixed part (see Fig. 10). At the same time, the reaction zone (V_R) also increases with increasing ϕ_j . Therefore, the proportion of the mainly premixed part remains almost constant at different ϕ_j for the WBB case.

5.3. Flame classification

To compare the NBB and WBB flame modes in a more fundamental way, we calculate the turbulent Reynolds number (Re_t) and the Damköhler number (Da) to draw the Borghi diagram [35] for the flame classification. The turbulent Reynolds number is defined as

$$Re_t = u' l_0 / \nu \quad (4)$$

where u' is the root-mean-squared fluctuation velocity, l_0 is the integral length scale and ν is the kinematic viscosity. Damköhler number (Da) is defined as the ratio of a characteristic flow time (τ_{flow}) to a characteristic chemical time (τ_{chem}), viz.,

$$Da = \frac{\tau_{\text{flow}}}{\tau_{\text{chem}}} = \frac{l_0 / u'}{\delta_L / S_L} \quad (5)$$

where δ_L and S_L are the laminar flame thickness and the laminar

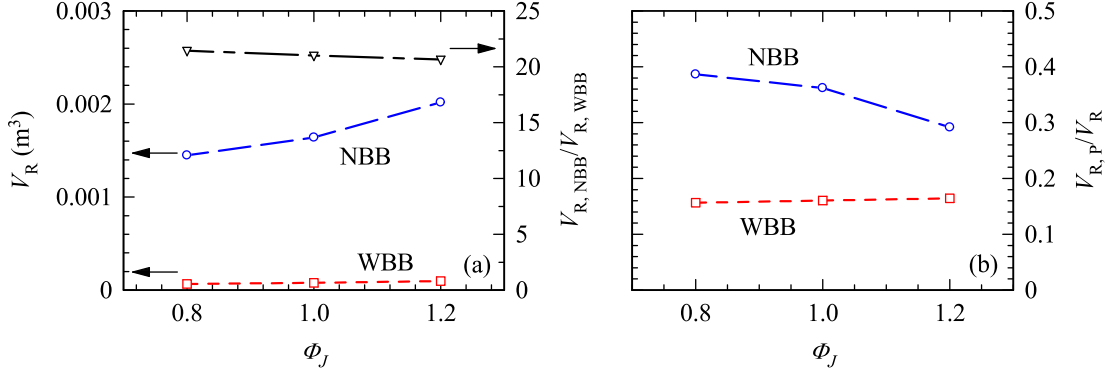


Fig. 11. (a) Reaction zone volume (V_R) for the NBB and WBB cases and ratio of NBB volume to WBB volume and (b) the proportion of mainly premixed reaction zone ($V_{R,P}/V_R$) for different cases.

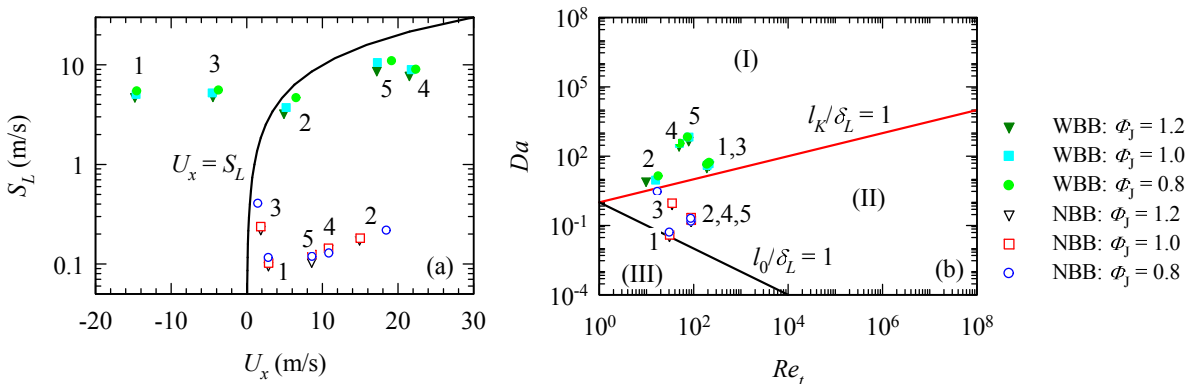


Fig. 12. (a) Laminar flame speed (S_L) against the local axial velocity (U_x) and (b) Damköhler number (Da) versus the turbulent Reynolds number (Re_t).

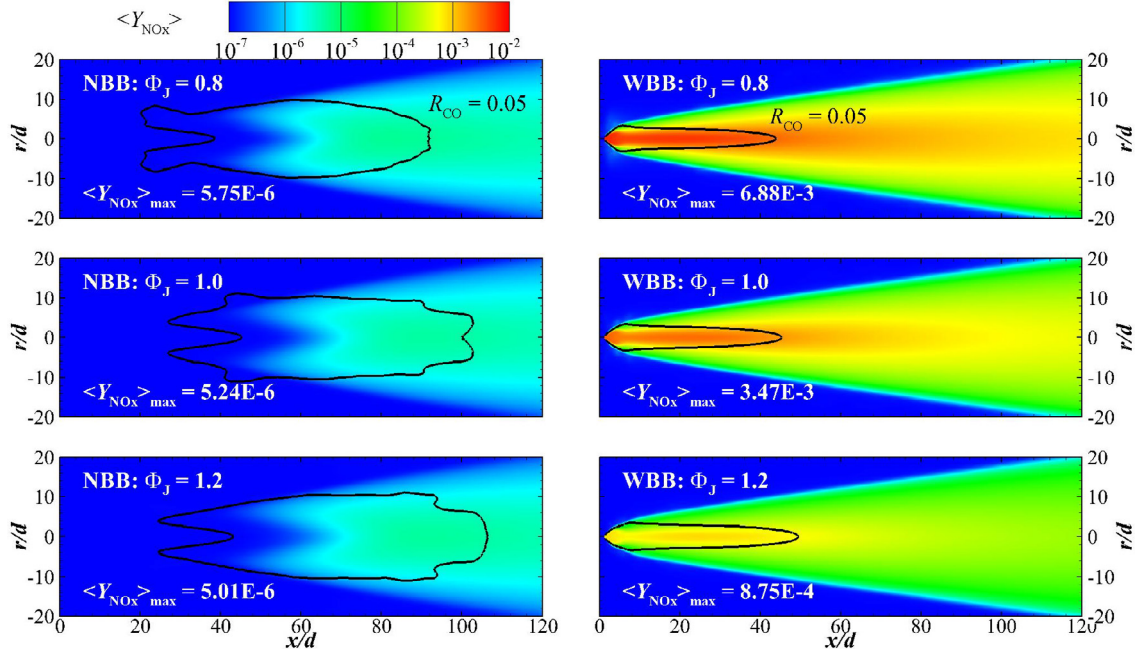


Fig. 13. Center-plane contours of Favre-averaged mass fraction of NO_x ($\langle Y_{\text{NO}_x} \rangle$) for the NBB and WBB cases. The black solid lines represent the boundary of the reaction zone. The maximum Favre-averaged mass fraction of NO_x ($\langle Y_{\text{NO}_x} \rangle_{\text{max}}$) is also shown in the contours.

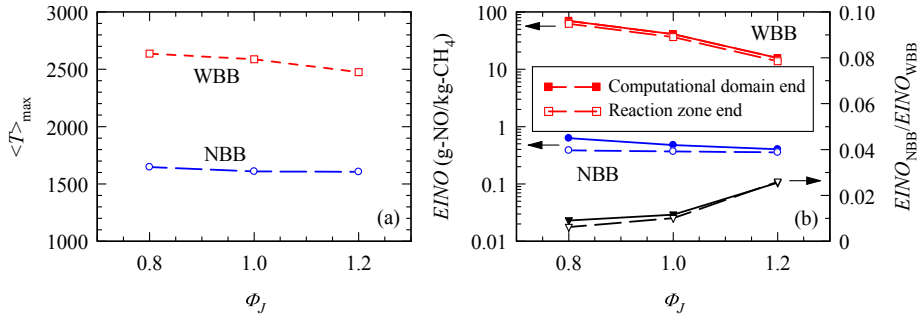


Fig. 14. The maximum Favre-averaged temperature $\langle T \rangle_{\text{max}}$ (a) and the NO_x emission index $EINO$ (b) against the jet equivalent ratio (Φ_J) for the NBB and WBB cases.

flame speed, respectively. Since we use the modified $k-\varepsilon$ model as the turbulent model, u' and l_0 can be calculated by

$$u' = \left(\frac{2k}{3} \right)^{1/2}, \quad l_0 = C_\mu k^{3/2} / \varepsilon \quad (6)$$

and δ_L can be estimated by

$$\delta_L = 2\alpha/S_L \quad (7)$$

where k is the turbulent kinetic energy, ε is the turbulent dissipation rate, C_μ is the constant of 0.09, and α is the thermal diffusion coefficient. All quantities can be obtained using the calculation results.

The remaining parameter for the flame classification is the laminar flame speed (S_L) which can be calculated using CHEMKIN-PRO [36]. We choose five representative positions (i.e., red dots in Fig. 8) in the reaction zone of each case for the flame classification. Fig. 12 displays the scatterplots of the laminar flame speed (S_L) against the local axial velocity (U_x) and Damköhler number (Da) against the turbulent Reynolds number (Re_t). For the NBB case, see Fig. 13a, the laminar flame speed (~0.1 m/s) is evidently lower than

the local flow speed, so the flame cannot be stabilized through flame propagation. For such a case, auto-ignition is the only way to establish and stabilize the 'flame', which is the MILD combustion, consistent with the previous work [18,37]. For the WBB case, among the selected five locations, there are two at $U_x < 0$, one where $S_L \approx U_x$, and two where $S_L < U_x$. Therefore, the conventional flame can be established by the 'pilot' flame due to the recirculation zone and by flame propagation.

For the premixed combustion, fundamentally, there are three reaction regimes: i.e., (I) reaction sheets, (II) flamelets in eddies and (III) distributed reactions. Fig. 12b illustrates these regimes by two solid lines and shows where the present cases are located. Above the red line of $l_k/\delta_L = 1$, chemical reactions occur in Regime (I); below the black line of $l_0/\delta_L = 1$, reactions occur in Regime (III). Between the two solid lines, combustion takes place in Regime (II), where the flame is broken into small pieces by large-scale eddies. Obviously, all the data points for the WBB case are located in Regime (I) with relatively high Da and strong turbulence. So chemical reactions are very fast and the flame thickness is quite small, smaller than the Kolmogorov scale. It follows that the WBB flame cannot be broken by any large or small eddies and maintains as continuous flame sheets. These flame sheets bend and twist

under the effect of large eddies and finally forming a wrinkle flame, which is well visible. Conversely, all the data points for the NBB case fall in Regime (II). Their turbulent Reynolds numbers are almost the same as for the WBB case while their $Da = 10^{-2}-10^0$, which is much lower than that for the WBB case. Their chemical reactions take place at moderate rates and thus the flame length scale is larger than the Kolmogorov scale but smaller than the integral scale. Under such conditions, the flame will be broken up into many small pieces by large eddies. This is also confirmed by the direct numerical simulations by Minamoto et al. [38,39]. They pointed out that the sheet-like structure dominates in the conventional flame while small flame pieces are most probably observed in the MILD combustion.

6. Distributions and emissions of NO_x

6.1. Global NO_x emission

[Fig. 13](#) presents the continuous contours of Favre-averaged mass fraction of NO_x ($\langle Y_{NOx} \rangle$), including NO and NO₂, for the NBB and WBB cases at $\Phi_J = 0.8, 1.0$ and 1.2. For the NBB case, NO_x is generated at $x \geq 45d$, later than the outset of the reaction zone. The temperature is low at the beginning of the reaction zone, so little NO_x is produced. When the temperature rises to a higher value after $x = 45d$, NO_x begins to accumulate, agreeing well with the previous work [40]. For the WBB case, NO_x mainly forms in the recirculation zone and just after the stagnation point, consistent with the measurements of Dally et al. [41]. It is also evident that for the NBB case, the NO_x levels are less than those of the WBB case with 2–3 orders of magnitude. This can be attributed to the lower temperature in the NBB case than in the WBB case. NO_x is strongly affected by the combustion temperature (exponential relationship) and will rise quickly with temperature $> 1800K$ [42]. Moreover, as Φ_J grows, $\langle Y_{NOx} \rangle$ decreases, especially for the WBB case. The reduction of temperature and the lowered oxygen level are the main reasons for the decreased NO_x formation. For the WBB case, there is a larger temperature drop (see [Fig. 14a](#)), so $\langle Y_{NOx} \rangle$ goes down faster, as Φ_J increases.

To quantify the NO_x emissions for the NBB and WBB cases, the emission index of NO_x [42] is defined as

$$EINO = \frac{m_{NOx, emitted}}{m_{F, burned}} \times 1000 \text{ (g - NO/kg - CH}_4\text{)} \quad (8)$$

The mass flux of the emitted NO_x is calculated at both the end of the reaction zone and the end of computational domain. The maximum Favre-average temperature ($\langle T \rangle_{max}$) in the whole computational domain and the NO_x emission index ($EINO$) versus Φ_J are demonstrated in [Fig. 14\(a\)](#) and (b), respectively. [Fig. 14a](#) shows that $\langle T \rangle_{max}$ is about 1600K for the NBB case and about 2500K for the WBB case. As a result, the NBB case can only produce the NO_x emissions of $EINO \leq 1$ (g-NO/kg-CH₄), less than 3% of those in the WBB case. Namely, the MILD combustion (the NBB case) emits extraordinarily low NO_x when comparing to the conventional combustion (the WBB case). It is also evident that $EINO$ is higher at the end of the computational domain than at the end of the reaction zone, especially at $\Phi_J = 0.8$. The high temperature N₂ and O₂ in the coflow guarantee the continuous NO_x formation downstream of the reaction zone. For $\Phi_J = 0.8$, the reaction zone is rather small and the temperature is quite high, thus N₂ and O₂ have more time to generate more NO_x in the downstream area of the reaction zone.

6.2. Relative importance of various NO_x formation mechanisms

Generally, there are four main formation mechanisms of NO_x during the combustion of hydrocarbon fuels that contain no nitrogen [42]: i.e., thermal-NO_x, prompt-NO_x, N₂O-intermediate and NNH routes. Moreover, in fuel-rich conditions, the NO_x-reburning route plays an important role in NO_x destruction. To study the relative importance of the five routes, the GRI-Mech 2.11 mechanism containing detailed NO_x formation and destruction mechanisms is adopted in this work, following our previous studies [43–45] (the detailed NO_x reactions are not presented here). We calculate NO_x from the five routes separately by performing calculations with each mechanism at a time.

[Fig. 15](#) presents the center-plane contours of $\langle Y_{NOx} \rangle$ from every route for the NBB and WBB cases with $\Phi_J = 1.0$. Since NO_x from the NO_x-reburning route is negative and inconvenient, the absolute value is given in [Fig. 16-a5](#) and 16-b5. Obviously, for the NBB case, the N₂O-intermediate route is the most significant mechanism for NO_x formation, consistent with Li et al. [13,43], while the NNH route is the second important one. Guo et al. [46,47] also reported that the two crucial routes of NO_x formation in the pure CH₄/air premixed flame are the N₂O-intermediate and the NNH routes. The initiation reactions of NNH \rightleftharpoons N₂ + H and NNH + M \rightleftharpoons N₂ + H + M are accelerated due to the higher concentration of H radical in the premixed flame comparing to that in the non-premixed flames. Therefore, different from the previous studies on non-premixed flames [40,44,45], the importance of NNH route is greatly intensified in the present premixed methane flames.

For the NO_x formation from the thermal route, the contradictory phenomena are observed in the two cases. It is very limited in the NBB case for the low temperature (about 1600K). For the WBB case, however, NO_x is mainly formed through the thermal route. The thermal route is the most sensitive mechanism to the temperature variation. The temperature in the WBB case is very high, up to 2600K, so the thermal route is immediately enhanced to the dominant mechanism. For both cases, the prompt mechanism contributes the least to the overall NO_x formation, consistent with Guo et al. [46,47]. Moreover, the NO_x-reburning mechanism has a great impact on the overall NO_x formation in the NBB case, but its influence on the WBB flame reduces. The reason is that the NO_x-reburning reactions of NO_x with hydrocarbon radicals (CH_i) are less efficient as the temperature increasing from 1600K to 2500K [44].

To further analyze the contributions of these five NO_x formation/destruction routes, we calculate the NO_x mass flux (m_{NOx}) from every route at different axial distance (x/d); the results are presented in [Fig. 16](#). For the NBB case, the significant formation of NO_x appears to occur from $x = 50d$, which results predominantly from the N₂O-intermediate ($\approx 50\%$) and NNH (45%) routes and much less from thermal and prompt routes ($< 10\%$ each). The NO_x-reburning is also an important mechanism for destruction of the formed NO_x (-22%). As x increases from $x = 50d$ to $x = 100d$, NO_x formations and destruction from all routes increase, forming the fastest growing region of the total NO_x. This region corresponds to the reaction zone. Farther downstream, the NO_x production from the N₂O-intermediate route continues to grow significantly as x increases. However, at $x > 100d$, NO_x products from NNH, thermal and prompt routes remain almost constant while that from the NO_x-reburning route continues to reduce. The initial reaction of N₂O-intermediate route N₂ + O \rightleftharpoons N₂O has a low activation energy and thus a lower temperature is favorable for this mechanism. Downstream from the reaction zone, the temperature decreases but NO_x from the N₂O-intermediate route still increases. This can also be confirmed in [Fig. 16-a2](#). The proportion of NO_x formation from the N₂O-intermediate route is a little bit lower than that from

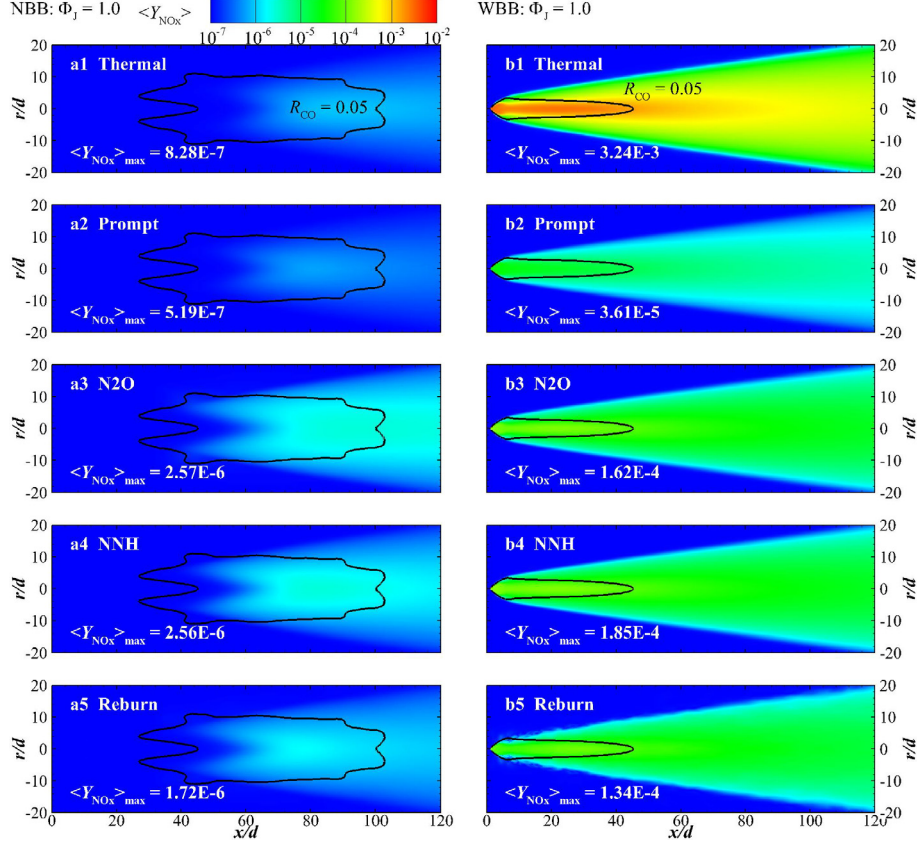


Fig. 15. Center-plane contours of Favre-averaged mass fraction of NO_x ($\langle Y_{NO_x} \rangle$) from thermal (a1, b1), prompt (a2, b2), N₂O-intermediate (a3, b3), NNH (a4, b4) and NO-reburning (a5, b5, absolute value) mechanisms for the NBB and WBB cases. Solid black lines represent the boundary of the reaction zone.

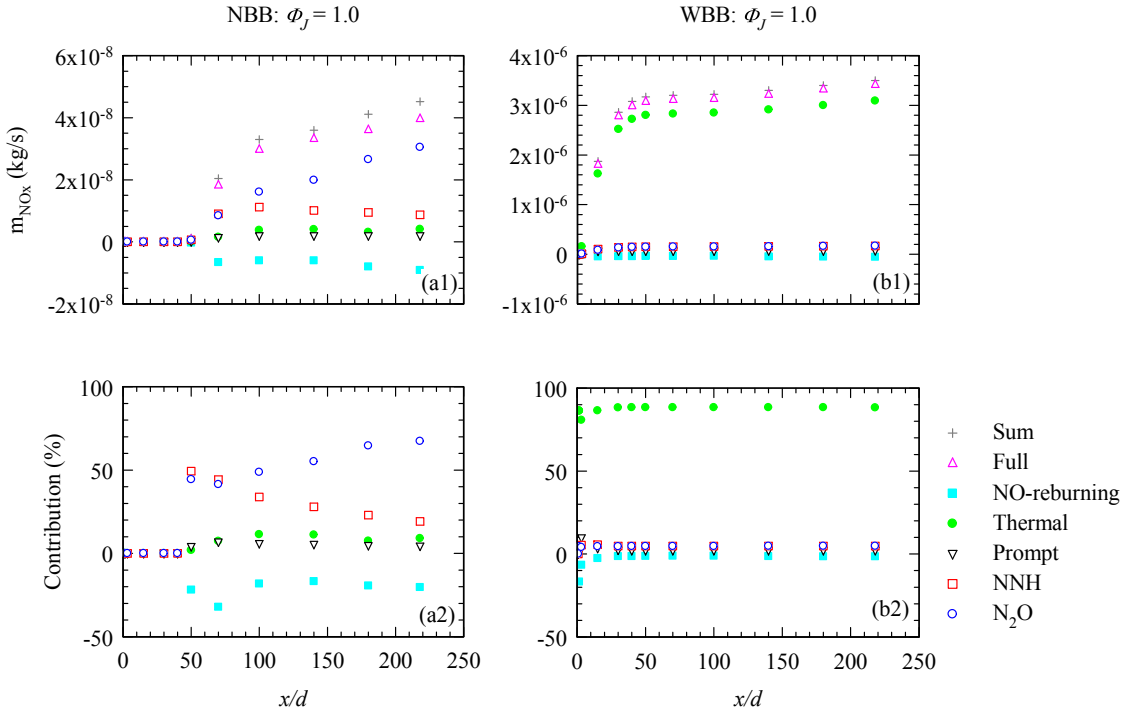


Fig. 16. Mass flux of NO_x (m_{NO_x} , a1, b1) and contributions of different mechanisms (a2, b2) against the axial distance (x/d) for the no-bluff-body (NBB: $\phi_J = 1.0$) and with-bluff-body (WBB: $\phi_J = 1.0$) cases.

the NNH route at $x = 50d$ and $70d$. Nonetheless, the proportion of N_2O -intermediate route is higher at $x > 100d$. The proportion of NO-reburning route is very significant ($>30\%$) at the beginning and reduces downstream, finally becoming constant (about 20%).

For the WBB case, the conventional flame starts to generate NO_x at a very small x and the NO_x mass flux has a sharp rise at $x = 1.5d$. The thermal route controls the overall NO_x formation, taking more than 80% contribution. The sum of contributions from other mechanisms (N_2O -intermediate, NNH and prompt) is less than 20%. In addition, the NO-reburning route makes a negligible contribution in the NO_x emission. As x increases, the NO_x formation/destruction from all routes increase and thermal route keeps dominant. The fastest growing region is from $1.5d$ to $30d$, corresponding to the reaction zone position. At $x > 30d$, the growing speed significantly slows down. This can be explained by the reduced temperature (of about 500K) and lack of radicals like O, H and OH, which play important roles in the NO_x formation [40].

For the WBB case, the thermal mechanism is always the dominant route at all values of Φ_J because of high combustion temperatures. Nonetheless, the situation is different for the NBB case. Fig. 17 shows the Φ_J dependences of NO_x emissions ($E\text{INO}$, calculated at the end of the reaction zone) from different mechanisms for the NBB case. As Φ_J increases, NO_x emissions from the N_2O -intermediate and thermal routes decrease, while those from NNH and prompt routes increase. The NO_x reduction from the NO-reburning route is also strengthened. This is understood when considering the variations of temperature and radicals. As Φ_J increases, the temperature drops a few degrees, so the NO_x production from the thermal route decreases. In addition, the O_2 level reduces with increasing Φ_J , so the concentration of O radical decreases and the concentrations of H and CH_i radicals increase. Therefore, the N_2O -intermediate route initiated by reactions of N_2 and O is depressed and the NNH route (and prompt route) initiated by reactions of N_2 and H (by reactions of N_2 and CH_i) are intensified. Moreover, the NO-reburning is also enhanced at the stoichiometric and fuel-rich conditions because of increasing CH_i . Finally, the overall NO_x emission changes little with Φ_J .

7. Concluding remarks

This work has been perhaps the first study that distinguishes the MILD combustion truly with the traditional bluff-body flame when keeping the same inlet and boundary conditions. Specifically, we have characterized the MILD combustion and its NO_x formation of a premixed methane jet flame in hot (1250 K) coflow against the conventional bluff-body counterpart. Detailed comparisons of their establishment processes of combustion, reaction-zone characteristics and NO_x distributions are made in Sections 4–6, from which several key conclusions can be drawn below:

- (1) For the non-bluff-body (NBB) case, the lifted MILD combustion 'flame' is established in the mixing layer far downstream from the nozzle exit. Conversely, for the with-bluff-body (WBB) case, the conventional flame is formed immediately downstream from the bluff body.
- (2) For the NBB case, the premixed MILD combustion is basically established through auto-ignition. The premixed jet is heated and diluted by the hot vitiated coflow at 1250 K, which is substantially higher than 813 K (auto-ignition temperature), and then ignition occurs spontaneously. Finally, a lifted MILD combustion 'flame' is stabilized at $x \geq 50d$. However, for the WBB case, the oncoming premixed reactants are continuously ignited by extremely hot combustion products (>2000 K) in the recirculating zone behind the bluff body, thus forming a traditional stable flame.
- (3) Relative to the traditional flame, MILD combustion reactions take place at much lower rates over a far larger reaction zone. The well premixed flame accounts for a large proportion in the MILD combustion and for a small portion in the traditional flame. In the latter, the partially premixed flame is dominant. As the jet equivalent ratio (Φ_J) increases, the reaction zone is enlarged for both combustion modes.
- (4) The laminar flame speed (S_L) is comparable with the local axial velocity (U_x) in the traditional flame while $S_L \ll U_x$ in the MILD combustion. Importantly, the MILD combustion is composed of many mini flamelets diffusing in large-scale eddies, with relatively small values of Damköhler number, i.e. $Da = 10^{-2}–10^0$. However, the traditional flame has much higher values of Da ($= 10^1–10^3$) and correspondingly falls into the regime of reaction sheets.
- (5) The MILD combustion produces extremely low NO_x emission, less than 3% of that from the traditional flame. In the MILD combustion, the main NO_x formation mechanisms are N_2O -intermediate and NNH routes while the NOx-reburning route is important for the destruction of NO_x . As Φ_J increases from 0.8 to 1.2, the contribution of N_2O -intermediate route reduces while those of NNH and prompt routes grow. The NOx-reburning destruction is intensified at the fuel-rich ($\Phi_J > 1$) condition. In contrast, for the conventional flame, more than 80% of NO_x emissions results from the thermal route at any Φ_J .

At last, we would also like to remark here on some practical issues of MILD combustion based on the present work. The MILD combustion occurs and sustains due to auto-ignition, which can be characterized particularly by high flow speed, weak reactions, low Da , uniform temperature and composition fields, and extremely low NO_x emissions. Accordingly, it differs greatly from the traditional bluff-body flame and should have advantages in numerous

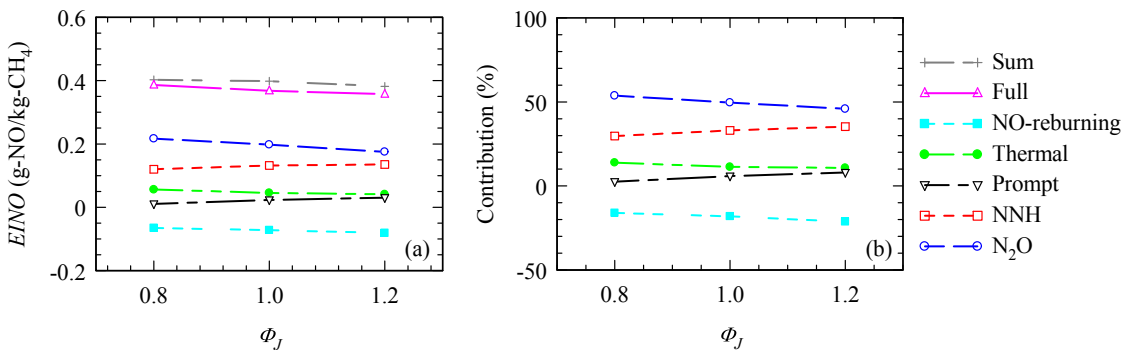


Fig. 17. (a) NOx emission index ($E\text{INO}$) and (b) contributions of different mechanisms against the jet equivalence ratio (Φ_J) for the NBB case.

industrial systems. For instance, this combustion is beneficial in furnaces or kilns of the process industry such as cement, glass and steel, etc., where combustion releasing heat transfers to the target internally, rather than through the furnace wall (of, e.g., water tubes). In these applications, uniform temperature distribution in the furnace is favorable for the heat treatment or melting procedures. Potentially, this combustion technology can also be utilized in stationary gas turbines and diesel engines, where combustion is initiated by auto-ignition. By using this technology, high thermal efficiency, low acoustic oscillations and low NO_x emissions will be achieved in these compact power or propulsion equipment. Nevertheless, such applications are still not in reality due to the difficulties of meeting all the engine requirements when operating in the MILD regime. Besides, the MILD combustion should be very suitable for the utilizations of wastes (industrial, agricultural and domestic wastes) and low calorific value fuels, like biogas, coke oven gas, blast furnace gas, etc. Problems of flame instability and quenching in traditional combustion are unlikely to occur in MILD combustion. In addition, this technology may be adopted in the stream reforming of hydrocarbon fuels, since the distributed reactions and uniform temperature and composition fields are favorable for producing CO and hydrogen efficiently.

On the other hand, it should be noted that, when designing MILD combustion furnaces, to gain a sufficiently high jet velocity and momentum, small nozzle diameters should be considered where possible. Rational nozzle arrangement and burner position are also important for tardy ignition of the combustible mixture as well as avoiding locally reaching high temperatures. Moreover, the furnace size could be considered smaller than that in traditional combustion because of elevated heat transfer rate, but the optimum furnace type (furnace length, width and height) should be adopted to guarantee the internal exhaust gas recirculation (EGR) conditions. Also, importantly, convective and radiative heat transfer on the wall or in the furnace should be seriously considered to keep the wall temperature higher than the auto-ignition temperature, since hot flue gas or hot wall is crucial for the spontaneous ignition of incoming reactants.

Acknowledgements

The authors greatly acknowledge the support of National Natural Science Foundation of China (No. 51776003) and High-performance Computing Platform of Peking University.

References

- [1] Cavaliere A, de Joannon M. Mild combustion. *Prog Energy Combust Sci* 2004;30(4):329–66.
- [2] Wünnigen J, Wünnigen J. Flameless oxidation to reduce thermal NO-formation. *Prog Energy Combust Sci* 1997;23(1):81–94.
- [3] Tsuji H, Gupta AK, Hasegawa T, Katsuki M, Kishimoto K, Morita M. High temperature air combustion: from energy conservation to pollution reduction. CRC press; 2002.
- [4] Katsuki M, Hasegawa T. The science and technology of combustion in highly preheated air. *Symposium (International) on combustion* 1998;27(2): 3135–46.
- [5] Perpignan AAV, Rao AG, Roekaerts DJEM. Flameless combustion and its potential towards gas turbines. *Prog Energy Combust Sci* 2018;69:28–62.
- [6] Som SK, Datta A. Thermodynamic irreversibilities and exergy balance in combustion processes. *Prog Energy Combust Sci* 2008;34(3):351–76.
- [7] Weber R, Smart JP, Kamp WV. On the (MILD) combustion of gaseous, liquid, and solid fuels in high temperature preheated air. *Proc Combust Inst* 2005;30(2):2623–9.
- [8] Szego GG, Dally BB, Nathan GJ. Scaling of NO_x emissions from a laboratory-scale mild combustion furnace. *Combust Flame* 2008;154(1–2):281–95.
- [9] Szego GG, Dally BB, Nathan GJ. Operational characteristics of a parallel jet MILD combustion burner system. *Combust Flame* 2009;156(2):429–38.
- [10] Mi J, Li P, Dally BB, Craig RA. Importance of initial momentum rate and air-fuel premixing on moderate or intense low oxygen dilution (MILD) combustion in a recuperative furnace. *Energy Fuels* 2009;23(11):5349–56.
- [11] Mi J, Li P, Zheng C. Impact of injection conditions on flame characteristics from a parallel multi-jet burner. *Energy* 2011;36(11):6583–95.
- [12] Mi J, Wang F, Li P, Dally BB. Modified vitiation in a moderate or intense low-oxygen dilution (MILD) combustion furnace. *Energy Fuels* 2011;26(1): 265–77.
- [13] Li P, Wang F, Mi J, Dally BB, Mei Z. MILD combustion under different pre-mixing patterns and characteristics of the reaction regime. *Energy Fuels* 2014;28(3):2211–26.
- [14] Kruse S, Kerschgens B, Berger L, Varea E, Pitsch H. Experimental and numerical study of MILD combustion for gas turbine applications. *Appl Energy* 2015;148:456–65.
- [15] Dally BB, Karpetis AN, Barlow RS. Structure of turbulent non-premixed jet flames in a diluted hot coflow. *Proc Combust Inst* 2002;29(1):1147–54.
- [16] Cabra R, Myhrvold T, Chen JY, Dibble RW, Karpetis AN, Barlow RS. Simultaneous laser Raman-Rayleigh-lif measurements and numerical modeling results of a lifted turbulent H₂/N₂ jet flame in a vitiated coflow. *Proc Combust Inst* 2002;29(2):1881–8.
- [17] Cabra R, Chen J, Dibble R, Karpetis A, Barlow R. Lifted methane-air jet flames in a vitiated coflow. *Combust Flame* 2005;143(4):491–506.
- [18] Gkagkas K, Lindstedt RP. Transported PDF modelling with detailed chemistry of pre- and auto-ignition in CH₄/air mixtures. *Proc Combust Inst* 2007;31(1): 1559–66.
- [19] Wang F, Mi J, Li P. Combustion regimes of a jet diffusion flame in hot co-flow. *Energy Fuels* 2013;27(6):3488–98.
- [20] Mei Z, Mi J, Wang F, Zheng C. Dimensions of CH₄-jet flame in hot O₂/CO₂ coflow. *Energy Fuels* 2012;26(6):3257–66.
- [21] Dai C, Shu Z, Li P, Mi J. Combustion characteristics of a methane jet flame in hot oxidant coflow diluted by H₂O versus the case by N₂. *Energy Fuels* 2018;32(1):875–88.
- [22] Kundu KM, Banerjee D, Bhaduri D. Theoretical analysis on flame stabilization by a bluff-body. *Combust Sci Technol* 1977;17(3–4):153–62.
- [23] Gkagkas K, Lindstedt RP, Kuan TS. Transported PDF modelling of a high velocity bluff-body stabilised flame (HM2) using detailed chemistry. *Flow, Turbul Combust* 2009;82(4):493–509.
- [24] Noor MM, Wandel AP, Yusaf TF. Analysis of recirculation zone and ignition position of non-premixed bluff-body for biogas MILD combustion. *Int J Automot Mech Eng* 2013;8(1):1176–86.
- [25] Bach E, Kariuki J, Dawson JR, Mastorakos E. Spark ignition of single bluff-body premixed flames and annular combustors. In: AIAA aerospace sciences meeting including the new horizons forum & aerospace exposition; 2013.
- [26] Christo FC, Dally BB. Modeling turbulent reacting jets issuing into a hot and diluted coflow. *Combust Flame* 2005;142(1–2):117–29.
- [27] Mei Z, Mi J, Wang F, Li P, Zhang J. Chemical flame length of a methane jet into oxidant stream. *Flow, Turbul Combust* 2015;94(4):767–94.
- [28] CT. Bowman, R.K. Hanson, D.F. Davidson, W.C. Gardiner, Jr, V. Lissianski, G.P. Smith, D.M. Golden, M. Frenklach and M. Goldenberg. http://www.me.berkeley.edu/gri_mech/.
- [29] Christo FC, Dally BB. Application of transport PDF approach for modelling MILD combustion. In: 15th australasian fluid mechanics conference; 2004. Sydney, Australia.
- [30] Pope SB. Computationally efficient implementation of combustion chemistry using in situ adaptive tabulation, vol. 1; 1997. p. 41–63.
- [31] Masri AR, Cao R, Pope SB, Goldin GM. PDF calculations of turbulent lifted flames of H₂/N₂ fuel issuing into a vitiated co-flow. *Combust Theor Model* 2004;8(1):1–22.
- [32] Chui EH, Raithby GD. Computation of radiant heat transfer on a non-orthogonal mesh using the finite-volume method. *Numer Heat Transf* 1993;23(3):269–88.
- [33] Bilger RW, Stärner SH, Kee RJ. On reduced mechanisms for methane-air combustion in nonpremixed flames. *Combust Flame* 1990;80(2):135–49.
- [34] Yamashita H, Shimada M, Takeno T. A numerical study on flame stability at the transition point of jet diffusion flames. *Symposium (International) on Combustion* 1996;26(1):27–34. Elsevier.
- [35] Borgioli R. On the structure and morphology of turbulent premixed flames. Recent advances in the Aerospace Sciences. Boston, MA: Springer; 1985. p. 117–38.
- [36] CHEMKIN-PRO 15131. Reaction design. 2013. San Diego.
- [37] Schulz O, Jaravel T, Poinsot T, Cuenot B, Noiray N. A criterion to distinguish autoignition and propagation applied to a lifted methane-air jet flame. *Proc Combust Inst* 2017;36(2):1637–44.
- [38] Minamoto Y, Dunstan TD, Swaminathan N, Cant RS. DNS of EGR-type turbulent flame in MILD condition. *Proc Combust Inst* 2013;34(2):3231–8.
- [39] Minamoto Y, Swaminathan N, Cant SR, Leung T. Morphological and statistical features of reaction zones in MILD and premixed combustion. *Combust Flame* 2014;161(11):2801–14.
- [40] Shu Z, Dai C, Li P, Mi J. Nitric oxide of MILD combustion of a methane jet flame in hot oxidizer coflow: its formations and emissions under H₂O, CO₂ and N₂ dilutions. *Fuel* 2018;234:567–80.
- [41] Dally BB, Masri AR, Barlow RS, Fiechtner GJ, Fletcher DF. Measurements of NO in turbulent non-premixed flames stabilized on a bluff body. *Symposium (International) on Combustion* 1996;26(2):2191–7. Elsevier.
- [42] Turns SR. An introduction to combustion. New York: McGraw-hill; 1996.
- [43] Li P, Wang F, Mi J, Dally BB, Mei Z, Zhang J, Parente A. Mechanisms of NO formation in MILD combustion of CH₄/H₂ fuel blends. *Int J Hydrogen Energy* 2014;39(33):19187–203.

- [44] Wang F, Li P, Zhang J, Mei Z, Mi J, Wang J. Routes of formation and destruction of nitrogen oxides in CH₄/H₂ jet flames in a hot coflow. *Int J Hydrogen Energy* 2015;40(18):6228–42.
- [45] Cheong KP, Li P, Wang F, Mi J. Emissions of NO and CO from counterflow combustion of CH₄ under MILD and oxyfuel conditions. *Energy* 2017;124: 652–64.
- [46] Guo H, Smallwood GJ, Liu F, Ju Y, Gülder ÖL. The effect of hydrogen addition on flammability limit and NOx emission in ultra-lean counterflow CH₄/air premixed flames. *Proc Combust Inst* 2005;30(1):303–11.
- [47] Guo H, Smallwood GJ, Gülder ÖL. The effect of reformate gas enrichment on extinction limits and NOx formation in counterflow CH₄/air premixed flames. *Proc Combust Inst* 2007;31(1):1197–204.